Research Article

Nanoconfinement geometry of pillared V_2O_5 determines electrochemical ion intercalation mechanism and diffusion pathway

Jameela Karol,[1,2] Charles O. Ogolla,[3] Manuel Dillenz,[4] Mohsen Sotoudeh,[4] Ellen Vollmer,[1,2]
Maider Zarrabeitia,[1,2] Axel Groß,[1,4] Benjamin Butz,[3] Simon Fleischmann[1,2*]

[1] Helmholtz Institute Ulm (HIU), 89081 Ulm, Germany
[2] Karlsruhe Institute of Technology (KIT), 76021 Karlsruhe, Germany
[3] University of Siegen, Micro- and Nanoanalytics Group, 57076 Siegen, Germany
[4] Institute of Theoretical Chemistry, Ulm University, Ulm, 89081 Germany
* Corresponding author's email: simon.fleischmann@kit.edu

Abstract

Improving electrochemical ion intercalation capacity and kinetics in layered host materials is a critical challenge to further develop lithium-ion batteries, as well as emerging cell chemistries based on ions beyond lithium. Modification of the nanoconfined interlayer space within host materials by synthetic pillaring approaches has emerged as a promising strategy, however, the resulting structural properties of host materials, host-pillar interaction, as well as evolving structure-functionality relations remain poorly understood. Herein, a series of bilayered V_2O_5 host materials pillared with alkyldiamine molecules of different lengths is systematically studied, resulting in tunable nanoconfinement geometry with interlayer spacings in the range of 1.0-1.9 nm. The electrochemical Li^+ intercalation capacity is increased from approx. 1 to 1.5 Li^+ per V_2O_5 in expanded host materials, and the intercalation kinetics improve with larger expansion. Operando X-ray diffraction reveals a transition of the charge storage mechanism from solid-solution Li^+ intercalation in V_2O_5 hosts with small and medium interlayer spacings, to cointercalation of Li^+ and solvent in V_2O_5 with the largest interlayer spacing. Density functional theory reveals a transition in Li^+ diffusion pathways from 1D to 2D diffusional networks for expanded interlayers. The work reveals the impact of nanoconfinement geometry within bilayered V_2O_5 on the resulting Li^+ intercalation properties, providing insights into both the microstructure and related functionality of pillared materials.

https://doi.org/10.26434/chemrxiv-2024-x5ggt **ORCID:** https://orcid.org/0000-0001-9475-3692

1. Introduction

The charge storage mechanism of lithium-ion batteries, as well as of novel cell chemistries beyond lithium, is based on electrochemical ion intercalation. The process involves the reversible storage of ions in a solid-state host electrode material that is typically undergoing small structural changes. Solid-state diffusion of the ions within the host lattice, as well as associated volumetric and/or crystallographic phase changes of the host itself, can limit the kinetics of the intercalation reaction. To realize high power charge storage processes, strategies to mitigate such limitations are being developed from an electrode perspective across length scales, from the macroscopic particle size scale down to the microscopic atomic arrangement within the host.[1–4]

Vanadium oxides are widely established as host materials for ion intercalation reactions. The bilayered V_2O_5 phase (δ-V_2O_5) is particularly versatile due to its ability to host a variety of cations, such as lithium, sodium, manganese, or zinc.[5,6] It can further be synthesized by several wet-chemical and hydrothermal methods, yielding a wide variety of attainable morphologies.[7] Thus, the material is suitable as a model system to explore electrochemical intercalation properties as a function of the host material structure and particularly its interlayer spacing.

An emerging concept to reduce kinetic limitations in host materials is the direct tuning of lattice parameters, such as the interlayer spacing of layered and two-dimensional materials, thereby modifying the nanoconfinement geometry within the host. Such tuning can be achieved via different functionalization approaches, including the insertion of pillars/spacer molecules into the host material structure.[8,9] It has been hypothesized that the resulting increased interlayer spacing in a layered intercalation host electrode can increase the ionic diffusion due to a reduced activation energy barrier for ion hopping between interstitial vacancy sites,[10] thereby allowing increased intercalation rates.

In the case of δ-V_2O_5, interlayer expansion was explored via ionic and/or molecular pillaring approaches. Clites et al. studied the chemical pre-intercalation of different sized alkali- and alkaline-earth ions as simple ionic pillars, resulting in a variation of the interlayer spacing between 0.96 – 1.34 nm.[11] The material with the largest initial interlayer spacing (δ-V_2O_5 pre-intercalated with Mg^{2+}) was found to exhibit the highest rate behavior for the electrochemical lithiation reaction.[11] Wei et al. pre-intercalated δ-V_2O_5 with Fe^{3+}-ions, which in turn improved the kinetics and stability of the electrochemical sodium intercalation reaction compared to pristine δ-V_2O_5. The authors attribute the effect to a large reduction in electrochemomechanical lattice breathing during (de-)sodiation.[12] In the tunnel-structured polymorph ζ-V_2O_5, pre-intercalation of Na^+ or K^+ led to an expansion of the 1D tunnels, yielding higher reversible lithium intercalation capacity and diffusivity.[13] Several ionic pillaring approaches of δ-V_2O_5 have also been reported to improve the capacity and stability of the electrochemical Zn^{2+} intercalation reaction, demonstrating the viability of the approach also for multivalent electrochemical intercalants in an aqueous electrolyte environment.[14–16] However, there is a need for a more systematic understanding of the impact of pillars on the charge storage mechanism, including the interaction between "pillaring ions" and mobile, electrochemically shuttled ions.

Beyond (monoatomic/simple) ions, molecules and/or polymers have been employed as pillars to tune the nanoconfined interlayer environment of V_2O_5.[17] These include polypyrrole or polyaniline, resulting in various reported V_2O_5 phases with a widened interlayer spacing (1.4 - 1.5 nm) and a variety of particle morphologies.[18–21] The studies demonstrate that the pillared materials exhibit improved electrochemical Zn^{2+} intercalation kinetics and stability compared to non-pillared V_2O_5, which was ascribed to "zero strain" volumetric behavior during cycling.[20] It was also found that the bonding nature and pillar mobility influence electrochemical Zn^{2+} intercalation.[22] Rotatable, covalently-bound terminal protons in the interlayer ("-OH pillars") provided superior kinetics for electrochemical Zn^{2+} intercalation compared to non-rotatable, ionically bound NH_4^+ pillars, even though the latter provided a larger interlayer spacing in V_2O_5.[22]

Overall, the studies suggest that pillaring of δ-V_2O_5 by simple ions or molecules is capable to improve capacity, kinetics, and/or stability of electrochemical ion intercalation reactions. However, there are large gaps in the mechanistic understanding of the structure and electrochemistry of such pillared host materials. Importantly, the interaction between pillars and host material (e.g., covalent / ionic / non-bonding) and associated changes in the host crystal structure upon pillar insertion, the local configuration of pillars, and the structural and chemical stability of the pillars during electrochemical cycling need to be identified. Due to the simultaneous variation of various parameters, the differentiation of the impact of the individual parameters like nanoconfinement geometry on the material performance is challenging. Furthermore, there is also a lack of understanding of the dependence of the intercalated ions' diffusion paths from the d-spacing of the host material, as alternative pathways could become activated in an expanded interlayer space. Computational studies are required that determine the diffusion paths and associated energy barriers as a function of the host materials' nanoconfinement geometry.[23,24]

To provide clear mechanistic insights and to systematically answer the raised questions about molecularly pillared host materials, a well-defined model system is required, which can unambiguously link the modulated nanoconfinement geometry to the electrochemical ion intercalation properties. This work presents a series of molecularly pillared δ-V_2O_5-alkyldiamine materials, which show a wide, systematic variation in interlayer spacing (1.0 – 1.9 nm) owing to different lengths of diamine pillars. The model systems exhibit an identical, well-defined intralayer crystal structure where only the *c*-parameter of the host system is varied by the molecular pillars. The materials possess comparable nanowhisker-morphology, specific surface area, pillar chemistry, and pillar density in the interlayer. This allows to link the observed electrochemical Li^+ intercalation properties to the nanoconfinement geometry in the host interlayer, utilizing combined electrochemical operando experiments and computational investigation of Li^+ diffusion paths and associated energy barriers. The work gives direct insights into the structural requirements for favorable ion intercalation properties in pillared V_2O_5 hosts. Moreover, much needed insights into the structure-property relationships of pillared host materials with a well-defined nanoconfinement environment is provided, being of interest to a wide audience including electrocatalysis[25] or selectivity[26].

2. Experimental

2.1 Materials synthesis

The alkyldiamine functionalized V_2O_5 was synthesized via hydro- and/or solvothermal synthesis routes in a 95 mL Teflon lined stainless-steel autoclave (BR-100, Berghof). The three alkyldiamines utilized are 1,2-ethylenediamine ($C_2H_8N_2$, 2C-DA, Sigma Aldrich), 1,6-hexanediamine ($C_6H_{16}N_2$, 6C-DA, ThermoFisher) and 1,12-dodecanediamine ($C_{12}H_{28}N_2$, 12C-DA, ThermoFisher). The molar ratio of alkyldiamine to vanadium used was 1:1. 0.3 g α-V_2O_5 powder (ThermoFisher) was added to 50 mL distilled water under constant stirring at room temperature. In the case of 12C-DA, a 1:1 volume ratio of distilled water and ethanol was used due to the low solubility of 12C-DA in water. The respective amounts of alkyldiamines were then added to the above solution with stirring. The pH value of the precursor solution was adjusted to 3 via the addition of 3 mol L^{-1} hydrochloric acid solution (Sigma Aldrich). The reaction mixtures were heated to 100 °C and held for 12 h, before naturally cooled to room temperature. The products were filtered through a PTFE filter paper (Whatman), washed with distilled water and ethanol, and then dried in an oven at 80 °C for 24 h.

$Li_xV_2O_5$ was synthesized via a sol-gel synthesis approach in accordance with earlier reports by Clites et al.[11] 2.33 g of LiCl (ThermoFisher) was added to 15 mL deionized water in a glass beaker with constant stirring. Subsequently, 15 mL of 30 wt.% H_2O_2 aqueous solution (Sigma Aldrich) was added. 0.5 g α-V_2O_5 was then slowly added to the solution under vigorous stirring. The Li:V molar ratio of 10:1 was used to ensure an excess of Li^+. The solution was stirred for 1 h at room temperature and subsequently heated to 60 °C with constant stirring for 3 h to form a dark red gel. The material was aged for four days at room temperature where the product precipitated in the form of a green powder. The product was dissolved in 3 M LiCl solution and hydrothermally treated at 220 °C for 24 h in the autoclave. Lastly, the sample was filtered through a PTFE filter paper, washed with deionized water, and dried at 80 °C for 24 h.

2.2 Physicochemical characterization

X-ray diffraction of powder samples was carried out using a Bruker D8 Advance diffractometer (Cu Kα radiation, $\lambda = 0.154$ nm) in the range of 2°-60° with a step size of 0.025° 2θ at a dwell time of 2 s per angular step. XRD of casted electrodes was performed using a polished Si-crystal holder and was measured in the same 2θ region with a step size of 0.04° 2θ at a dwell time of 14 s per step.

X-ray photoelectron spectroscopy (XPS) was performed on the pristine powders using a SPECS XPS system, equipped with a monochromatic Al Kα X-ray source ($h\nu$ = 1487 eV) and PHOIBOS 150 spectrometer. High-resolution scans of the C 1s, O 1s, V 2p and N 1s transitions were acquired at 400 W, 30 eV pass energy, and 0.1 eV energy step. Calibration of the binding energy was carried out using the adventitious carbon signal in the C 1s region (C-C/C-H) at 284.8 eV as a reference.[27] The collected spectra were fitted by CasaXPS software using a nonlinear Shirley-type background and a 70 % Gaussian / 30 % Lorentzian line shape.[28]

Thermogravimetric analyses (TGA) were carried out in the temperature range from room temperature to 550 °C at a heating rate of 5 K min^{-1} under constant oxygen flow in aluminum crucibles loaded with *ca.* 8 mg of material using a TGA209 F1 Libra (Netzsch).

Gas sorption measurements were carried out with an advanced micropore size and chemisorption analyzer (Quantachrome Instruments). The samples were outgassed at 80 °C under vacuum for 22 h before the measurement was carried out under argon gas. The ASiQwin software from Quantachrome was utilized to analyze the data.

2.3 Electron microscopy

Scanning electron microscopy (SEM) at 5 kV was applied to the powder samples on carbon tape using a Zeiss Crossbeam microscope. A Thermo Fisher/FEI Talos F200X transmission electron microscope (TEM) was utilized to perform bright-field TEM imaging (BFTEM), selected-area electron diffraction (SAED), as well as high-resolution TEM (HRTEM) imaging to prove sample quality and homogeneity, and to in detail characterize the sample morphology, crystal structure, and molecular spacer bilayer separation distance/spacing of the synthesized materials. The microscope, equipped with a high-brightness XFEG gun, was operated at 200 kV and column vacuum, beam current and imaging/capture times (frame integration) were optimized to keep beam damage of the samples at a minimum. The as-synthesized powder samples were dispersed onto TEM support grids (Plano S166-2). To separate the aggregated whiskers, small amounts of the aggregated powder were separated by gently grating two microscope glass slides against each other with the powder placed in between. The materials were dry transferred onto the TEM grids. Larger agglomerates were removed leaving clean scanty material suspended on the grid. Series of SAED patterns, as well as HRTEM images, were sequentially collected and integrated to minimize the applied beam-current density. To analyze the SAED patterns, JEMS software package (by P. Stadelmann, jems-swiss) was employed for pattern simulation and indexing. For precise determination of *c*-axis lattice constants, average radial intensity profiles were determined and the peak positions particularly of the (001) rings were extracted from the second-order derivative of the radial plot profiles.

2.4 Electrode preparation

The electrodes were fabricated using a slurry with a composition of 80:10:10 wt.% active material to carbon black (Super C65, C-NERGY) to polyvinylidene fluoride (PVDF, Solef 6020, Arkema Group) in N-methyl-2-pyrrolidone solvent (NMP, anhydrous, Sigma-Aldrich, 2 wt.% of PVDF in NMP). The slurries were mixed in a planetary speed mixer (Thinky, ARE-310) for 5 minutes at 2000 rpm and then cast on a carbon coated aluminum foil (20 µm, battery grade, Welcos), using a laboratory doctor blade with a wet film thickness of 60 µm. The electrode sheets were dried at 80 °C overnight (Binder ED-115 oven), and 12 mm diameter electrodes were cut with a hand puncher (Hohsen). Each disc electrode was weighed to determine the active material mass loading, which was kept low around 0.80±0.20 mg/cm^2 to minimize the influence of electrode architecture on the electrochemical performance. This was followed by another drying step at 80 °C under vacuum for 16 h before transfer to the glovebox.

2.5 Electrochemical characterization

Electrochemical characterization was carried out using 2032 type coin cells (Hohsen), which were assembled in an argon-filled glovebox (MBraun, O_2 & H_2O < 0.1 ppm). They contained a stack composed of the V_2O_5 electrodes on aluminum current collectors, a glass fiber separator (19 mm diameter, GF/A, Whatman), a 12 mm diameter lithium disc (500 µm thickness, Honjo), a stainless-steel spacer and a spring. As electrolyte, 90 µL of 1.0 M $LiPF_6$ in ethylene carbonate/diethyl carbonate is used (EC:DEC, 3:7 volume ratio, Powerlyte). All electrochemical experiments were performed in climatic chambers (Binder) at 20 °C with potentiostats from Biologic (VMP3, VMP-3e, VMP-300). Cyclic voltammetry (CV) and galvanostatic cycling were conducted in the potential window of 2.0 – 4.0 V vs. the Li^+/Li. For long-term cycling, a specific current of 500 mA/g was employed. To test the rate capability, specific currents of 20, 50, 100, 200, 500, 1000, 5000 mA/g were applied for 5 cycles each and the last 5 cycles were again run at 20 mA/g. All normalizations are with respect to combined mass of V_2O_5 with molecular pillar, unless explicitly stated otherwise.

2.6 Computational details

Density functional theory (DFT) was employed to study the influence of the d-spacing on the Li^+ diffusion barriers in bilayered V_2O_5. First, a benchmark of DFT functionals was conducted using the generalized gradient approximation (GGA) with the Perdew-Burke-Ernzerhof (PBE)[29] functional, the non-empirical strongly constrained and appropriately normed (SCAN)[30] meta-GGA functional, and the hybrid Heyd-Scuseria-Ernzerhof (HSE) functional (α=0.25)[31,32] within the projected augmented wave (PAW) method[33,34] as implemented in the Vienna ab initio simulation package (VASP). The third generation (D3)[35] semi-empirical van der Waals corrections proposed by Grimme and the revised Vydrov–van Voorhis (rVV10) nonlocal correlation functional,[36,37] respectively, were integrated into the structure optimizations. In addition, the influence of including Hubbard-type correction to accurately depict the behavior of localized d-electrons on the structural parameters was tested with the datadriven Hubbard U values of U_{PBE}=3.25[38] and U_{SCAN}=1.0[39]. The benchmarking of the DFT functional employed in this study is presented in **Table S1** of the Supporting Information. The plane-wave cutoff energy was set at 520 eV, with Monkhorst-Pack (MP)[40] k-point meshes of 3 × 3 × 3 representing the Brillouin zone. Activation barriers and minimum energy paths for carrier hopping were determined by the climbing image nudged elastic band (cNEB) method.[41,42] The diffusion path was first constructed by linear interpolation of atomic coordinates between initial and final states with five distinct images, followed by relaxation until the forces on all atoms were below 0.01 eV $Å^{-1}$. In the cNEB computations, the total energies were assessed using the SCAN+rVV10 functional, without incorporating any U corrections. Large supercells were used to ensure ion isolation from periodic images (ions separated by at least 10 Å). Initial atomic configurations were obtained from the Materials Project (MP) database.[43]

3. Results and discussion

3.1 Structural investigation

The goal of this work is to unambiguously link nanoconfinement geometry of a layered host electrode material, bilayered V_2O_5, with the resulting electrochemical ion intercalation properties. For this purpose, model electrode materials with different, well-defined interlayer spacings are synthesized by employing alkyldiamines of various lengths that act as molecular pillars/spacers within the interlayer. As illustrated in **Fig. 1**, ethylenediamine (2C-DA), 1,6-hexanediamine (6C-DA), or 1,12-dodecanediamine (12C-DA) are dissolved in water (water/ethanol mixture in case of 12C-DA for better solubility) together with commercially available α-V_2O_5 powder and undergo hydrothermal treatment at 100 °C for 12 hours in an autoclave. For further comparison, a reference sample with pre-intercalated Li^+ and H_2O (Li-V_2O_5) is synthesized via a sol-gel process followed by hydrothermal treatment, as described by Clites et al.[11] (**Fig. 1** and **Fig. S1**).

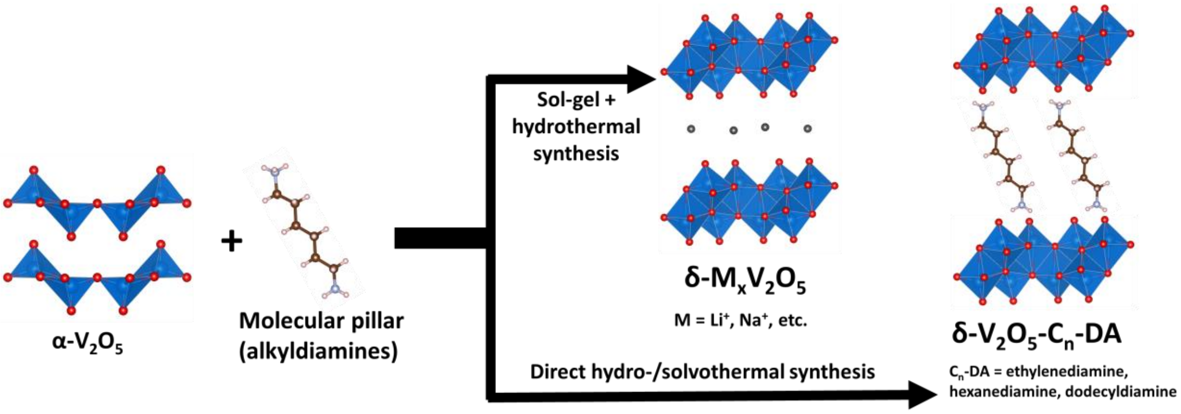

Figure 1: Illustration of the synthesis procedure of alkyldiamine-pillared, bilayered V_2O_5 samples.

Fig. 2A shows the powder XRD patterns of the alkyldiamine-pillared vanadium oxides used to determine the crystal structure and interlayer spacing of the synthesized materials. The diffractograms indicate that all three alkyldiamine-pillared V_2O_5 samples exhibit the main characteristic peaks corresponding to bilayered δ-V_2O_5, according to the structural model proposed by Petkov et al.[44] This includes peak maxima at 26.1° and 50.7° 2θ related to the (110) and (020) reflections, respectively. The different (001) diffraction angles of the three samples located at 8.7° (2C-DA), 7.3° (6C-DA), and 4.6° 2θ (12C-DA), demonstrate the successful tailoring of the interlayer spacing of V_2O_5 bilayers using different length alkyldiamine pillars. The corresponding (001) spacings derived from XRD are 1.01 nm (2C-DA), 1.21 nm (6C-DA) and 1.92 nm (12C-DA). Li-V_2O_5 synthesized via the sol-gel route exhibits the same crystal structure with a (001)-spacing of 1.22 nm (**Fig. S1B**), which is in the typical range of bilayered V_2O_5 materials with nanoconfined water and/or alkali cations.[7,11] A more detailed structural analysis of the bilayered V_2O_5 host structure is performed by highly localized transmission electron imaging/diffraction techniques, vide infra.

Linear fitting of the measured (001) spacings over the number of carbon atoms in the pillars' alkyl-chains demonstrates positive correlation (**Fig. 2B**). The arrangement of alkyldiamine pillars within the V_2O_5 host structure is approximated by geometrical considerations (**Fig. 2B**, inset), in accordance with previous work on pillared layered/2D materials.[45,46] These approximations base on the assumptions that (1) most alkyldiamines interact with V_2O_5 bilayers at both opposing sides of the interlayer galleries via their functional amine/ammonium groups, i.e., form "bridges" between the layers as described for insertion of alkyldiamines into clays under acidic conditions.[47] Further, (2) the alkyl-chains are assumed in a straight conformation (not bent or twisted), and (3) the molecule lengths are approximated by their van der Waals radii given an electrostatic pillar-host interaction. With alkyldiamine molecular lengths of 0.67 nm (2C-DA), 1.22 nm (6C-DA), and 2.1 nm (12C-DA) and a V_2O_5 bilayer thickness of 0.62 nm, the molecules are assumed to assemble with tilt angles α_i of 35°, 29°, and 38°, respectively, with respect to the bilayer direction (**Fig. 2B**, inset).

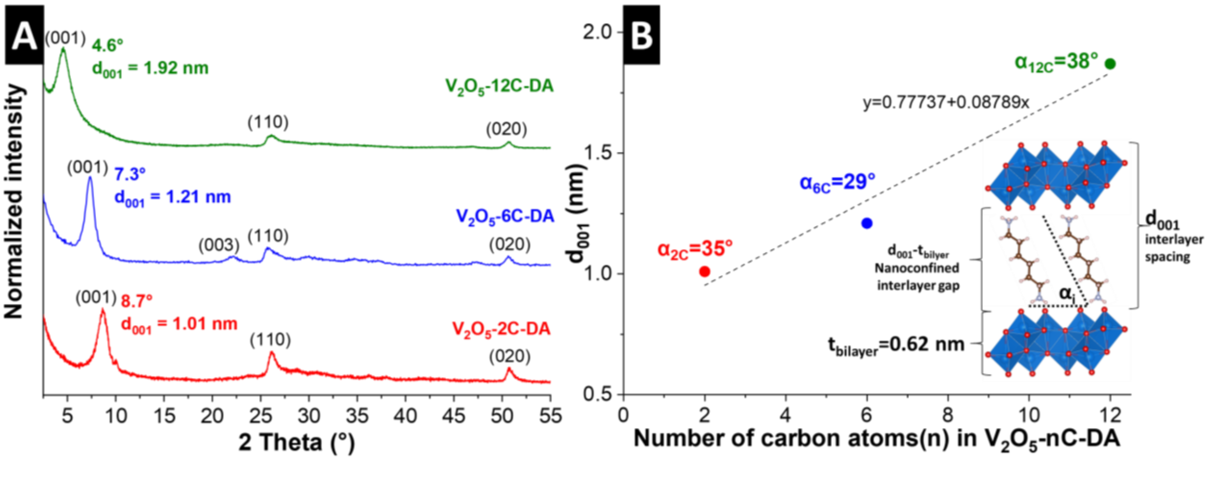

Figure 2: (A) X-ray diffractograms (Cu Kα, λ = 1.5406 Å) of alkyldiamine-pillared, bilayered V_2O_5 samples. Data is normalized to the highest peak intensity. (B) d-spacing calculated from the 2θ position of the (001) reflection as a function of the number of carbon atoms in the used alkyldiamine pillar including linear fit. Inset of bilayered V_2O_5 structure illustrates geometrical relation between d-spacing (d_{001}) from XRD signal, interlayer space and the tilt angle α_i of the pillars, assuming a linear conformation of the molecules.

An in-depth correlative microscopy investigation of the synthesized samples with variable nanoconfinement geometry is undertaken to elucidate the pillar-induced changes in the host structure. Scanning and transmission electron microscopy (SEM and TEM) are leveraged to confirm the materials' homogeneity, to gain insights into their morphology, to assess crystallinity and to verify the crystal structure (**Fig. 3**). All the molecularly pillared samples (V_2O_5-2C-DA, V_2O_5-6C-DA and V_2O_5-12C-DA) show characteristic nanowhisker morphology (SEM: **Fig. 3A-C**, TEM: **Fig. 3D-F**), allowing for individual free-standing strands to be investigated further. The V_2O_5-12C-DA system shows stronger bundling/agglomeration of the whiskers (**Fig. 3C and 3F**) compared to V_2O_5-2C-DA and V_2O_5-6C-DA, which is attributed to the solvent modification (ethanol-water mixture instead of only water, which is necessary to adequately dissolve 1,12-dodecanediamine).[48,49] TEM bright-field imaging (**Fig. 3D-F**) verifies the sample homogeneity and single-crystalline nature of the whiskers with low defect density. The nanowhiskers of high aspect ratio are found to be a few tens of nanometers wide and a few up to tens of micrometers long. Overall, the nanowhisker morphology of all samples is similar. This is a significant requisite to correlate the electrochemical Li^+ intercalation performance to the nanoconfinement geometry of the model materials, given that the morphology may have a significant influence on the electrochemical properties of V_2O_5.[50,51]

While sharing an unambiguous nanowhisker morphology with the (001) basal planes being systematically aligned parallel to the long whisker dimension (**Fig. 3J-L**), significant differences of interlayer spacing are revealed between the samples, attributed to the successful pillaring of the bilayered V_2O_5 host structure using alkyldiamine of three lengths. This is concluded from powder X-ray diffraction (XRD), selected-area electron diffraction (SAED) and high-resolution TEM (HRTEM) analyses (**Figs. 2A**, **3G-I**, **3J-L**, respectively). Complementary to the XRD, the crystal structure of the samples is confirmed by powder SAED of representative whisker ensembles. All three samples present a monoclinic crystal structure of the space group *C2/m* characteristic of such bilayered δ-V_2O_5 systems.[44] Comparing simulated with measured SAED pattern of the three samples, it becomes clear that a systematic increase in the (001) lattice spacing from 0.95 nm to 1.10 nm to 1.50 nm is observed for 2C-DA, 6C-DA and 12C-DA, respectively (**Fig. 3G,H**). However, the prominent SAED signals corresponding to (020) and (110) planes are identical for all samples, demonstrating no pillar-induced alteration of in-plane host structure (**Fig. 3H**). It should be noted that the smaller (001)-spacing derived from TEM analysis compared to XRD analysis may likely result from partial pillar degradation under the high energy electron beam and/or loss of confined interlayer species under vacuum conditions, although measures like minimal-dose imaging/diffraction were applied.[52,53] Nonetheless, the basal planes are continuous, well aligned and extend along the whole whisker. Moreover, the interlayer spacing within individual whiskers appears to be constant. Extended defects like kinks, cracks, discontinuities, grain boundaries or dislocations are rarely observed (**Figs. 3D-F, 3J-L**) proving the high quality of the synthesized materials. The *c*-parameters obtained from SAED are confirmed by localized HRTEM (insets of **Fig. 3J-L**). The results confirm that the employed alkyldiamine pillaring approach successfully leads to a variation of the V_2O_5 nanoconfinement geometry, while no changes in intralayer structure and morphology are observed.

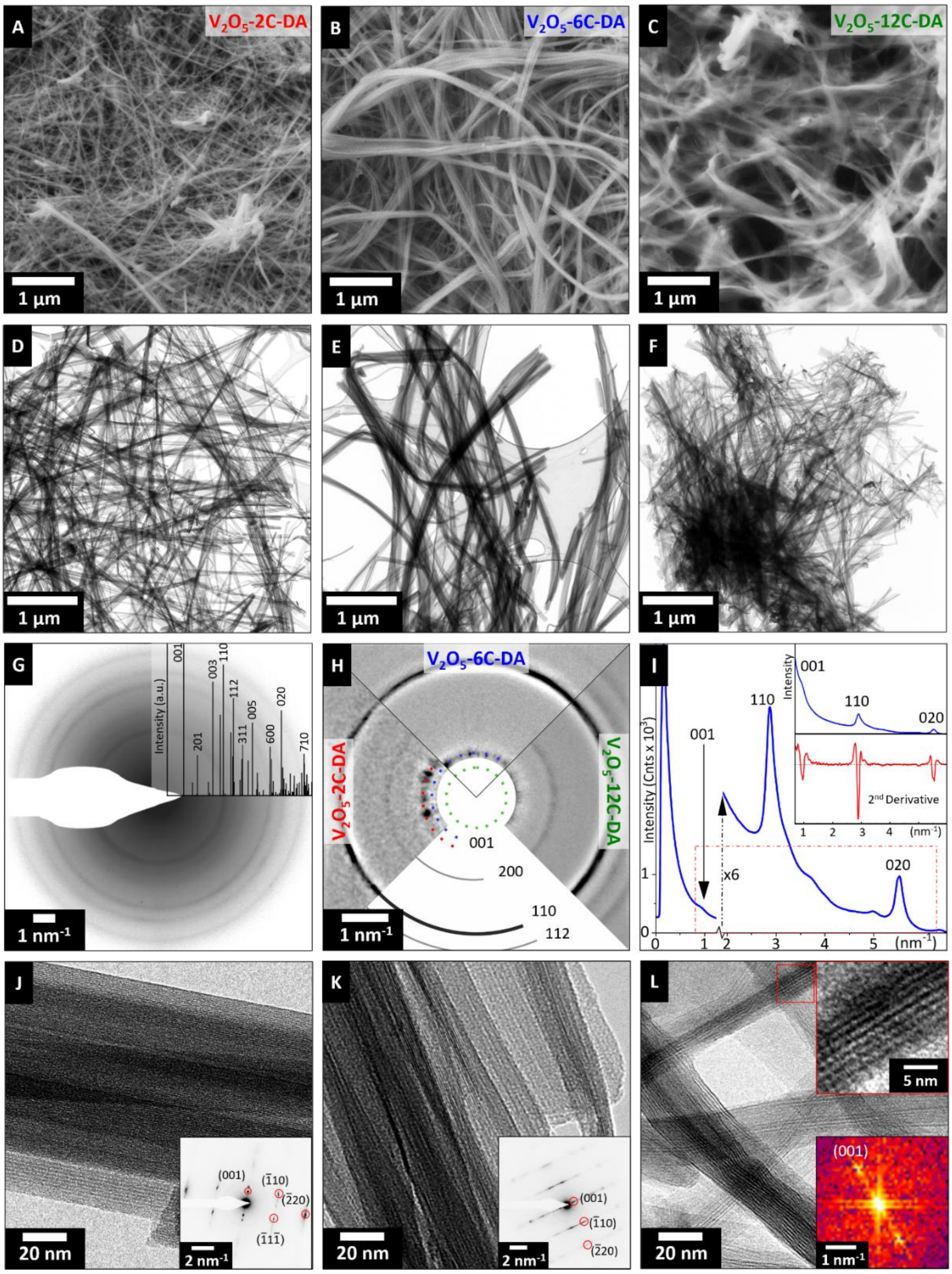

Figure 3: Morphology, microstructure, and crystal structure analyses by SEM and TEM: SEM images of (A) V_2O_5-2C-DA, (B) V_2O_5-6C-DA and (C) V_2O_5-12C-DA; (D)–(F) respective BFTEM images; (G) representative powder SAED (logarithmic display) of V_2O_5-12C-DA with simulation (structural model by Petkov et al.[44]) confirming the high degree of crystalline order; (H) comparison of SAED pattern centers (logarithmic display) with molecular spacer-dependent rings of (001) reflections in relation to the constant (200)/(110) rings; (I) quantitative determination of (001) spacings from patterns in (H) by azimuthal averaging (radial intensity plot) and peak background correction by second-order derivative calculation; (J)–(L) representative HRTEM micrographs with corresponding single-crystal SAED patterns (insets) of individual wires. In (L), the power spectrum (FFT) is displayed instead due to the (001) peak being located in close vicinity to the beam blocker.

The pillar content of the samples is analyzed by means of thermogravimetric analysis (TGA). Heating to 550 °C under a constant oxygen flow leads to the thermal decomposition and/or burn-off of any organic components in the V_2O_5 samples (caution: temperatures above ca. 600-650 °C should be avoided in these TGA experiments due to the low melting temperature of V_2O_5). The mass loss upon heating of the V_2O_5-alkyldiamine samples occurs mainly in two steps, as shown in **Fig. 4A**. The mass loss below ca. 150 °C is attributed to the loss of surface water and/or crystal water in the interlayer space.[54] This mass loss corresponded to ca. 5 wt.%, 3.5 wt.%, and 2 wt.% for V_2O_5-2C-DA, V_2O_5-6C-DA, and V_2O_5-12C-DA, respectively. The second step between ca. 200-400 °C, accounting for a subsequent mass loss of 8 wt.%, 9.7 wt.%, and 16.5 wt.% for V_2O_5-2C-DA, V_2O_5-6C-DA, and V_2O_5-12C-DA, respectively, is ascribed to the decomposition and/or burn-off of the alkyldiamine pillars.[55] This leads to calculated chemical compositions of the samples as V_2O_5-$(2C\text{-}DA)_{0.29}$, V_2O_5-$(6C\text{-}DA)_{0.18}$, and V_2O_5-$(12C\text{-}DA)_{0.19}$. While the molar ratio of educts in the reactions is chosen as 1:1 for alkyldiamine to vanadium, the TGA experiments reveal a product composition with significantly less pillars. The ratio of alkyldiamine pillars in the products is comparable for all samples, with a slightly higher number for 2C-DA, which is explained by its small size and low boiling point that allows for higher mobility during the synthesis.

To analyze the specific surface area and porosity of the samples, argon gas sorption measurements (GSA) are performed as shown in **Fig. 4B**, and the specific surface area of the samples is calculated using the Brunauer-Emmett-Teller (BET) equation.[56] The BET surface area is calculated to be 40 m^2/g for V_2O_5-2C-DA, 57 m^2/g for V_2O_5-6C-DA and 37 m^2/g for V_2O_5-12C-DA. All sorption isotherms exhibit a Type II shape without significant hysteresis, according to IUPAC classification, indicating non-porous or macroporous character of all samples.[57] It is notable that the expanded interlayer space, even in the case of V_2O_5-12C-DA, appears inaccessible for gas sorption. The GSA analysis confirms a comparable surface area and porosity for all samples.

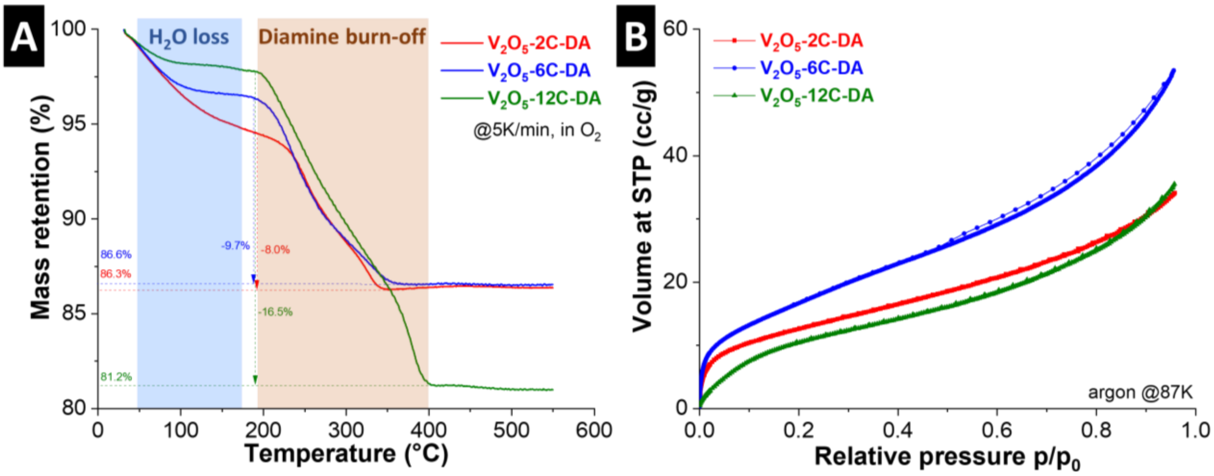

Figure 4: (A) Thermogravimetric analysis (TGA) of all samples in oxygen atmosphere at a heating rate of 5 K/min. (B) Argon sorption isotherms of all samples measured at 87 K (STP=standard temperature and pressure).

The interaction between the pillaring alkyldiamine molecules and the V_2O_5 host is analyzed by X-ray photoelectron spectroscopy (XPS). Both the O 1s and V 2p signals of all alkyldiamine-pillared samples are shown in **Fig. 5A-C**. Two signals corresponding to the spin-orbit of V $2p_{3/2}$ and V $2p_{1/2}$ are located in the energy ranges around 517 and 525 eV, respectively, which contain contributions of V(V) and V(IV).[58,59] This shows that surface vanadium in the alkyldiamine-pillared V_2O_5 samples is partially reduced after the chemical synthesis. The N 1s signals (**Fig. 5D-F**) show the main signal centered at 401.5 eV for V_2O_5-2C-DA, 401.2 eV for V_2O_5-6C-DA, and 401.8 eV for V_2O_5-12C-DA, which can be assigned to a positively charged nitrogen, such as $-NH_3^+$.[60] Hence, most pillar functional groups form cationic ammonium groups in the aqueous reaction solution, which interact by ionic bonding with the V_2O_5 host. The main N 1s signal of the three samples displays a shoulder at a lower binding energy of 399.3 eV that have been described for $-C-NH_2$,[61,62] indicating the simultaneous presence of small amounts of neutral alkyldiamine, which can be assumed as non-interacting with the V_2O_5 host via ionic or covalent bonds. Overall, XPS results demonstrate the predominantly ionic interaction between partially reduced V_2O_5 host and cationic ammonium groups, while a small residue of non-interacting amine groups is also found.

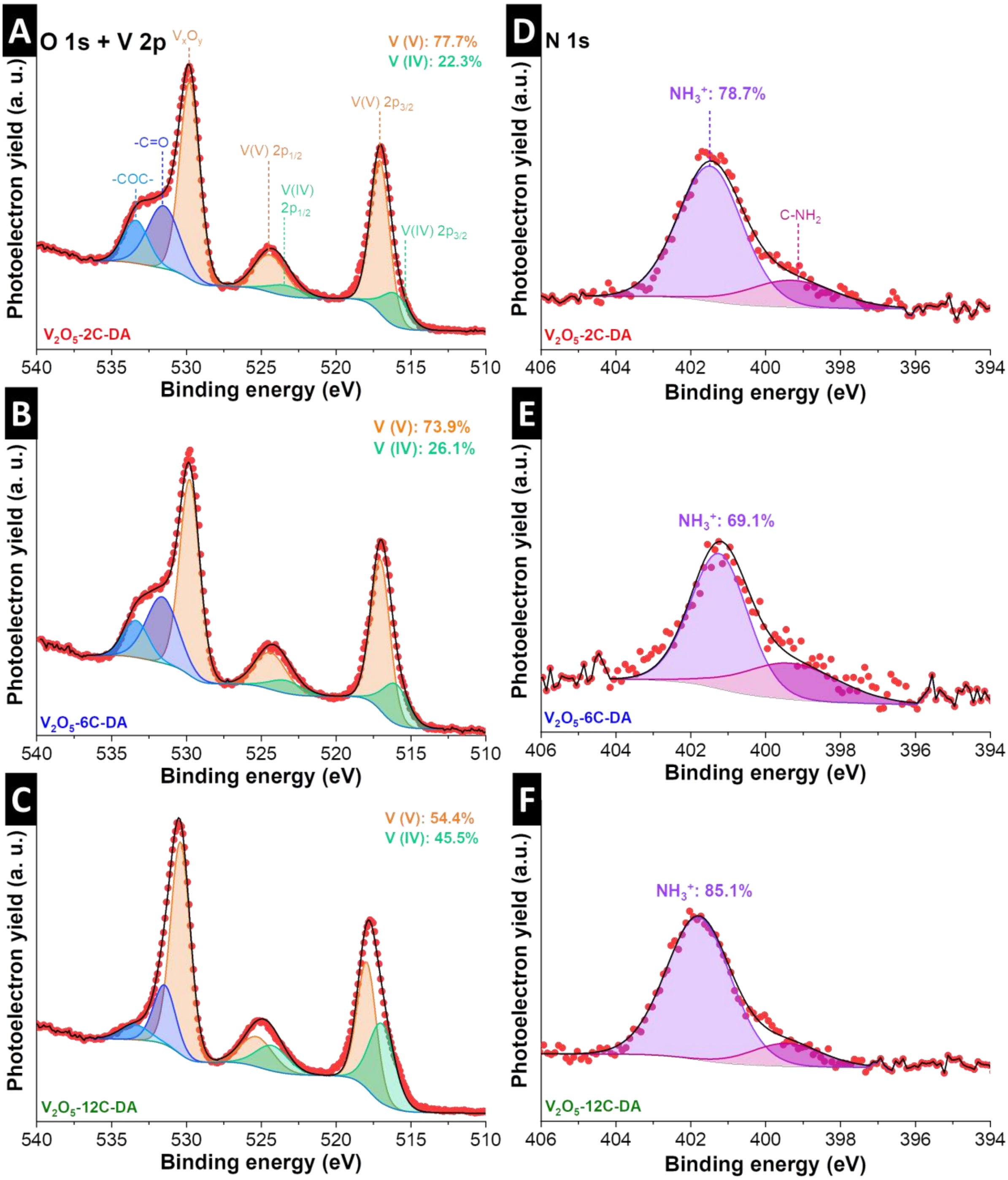

Figure 5: O 1s, V 2p and N 1s photoelectron lines of (A, D) V_2O_5-2C-DA, (B, E) V_2O_5-6C-DA and (C, F) V_2O_5-12C-DA.

3.2 Electrochemical characterization

Bilayered V_2O_5 materials are synthesized with three different nanoconfinement geometries by using alkyldiamine pillars with variable lengths. The structural investigation demonstrates that they exhibit highly comparable morphology, surface area, intralayer crystal structure, density of pillaring molecules in the interlayer, and ionic pillar-host interaction. Hence, they are suitable as model electrode materials to analyze the impact of the nanoconfinement geometry / interlayer spacing on the electrochemical Li^+ intercalation reaction, because influences of other structural features on the electrochemical signal remain negligible across the three samples.

Galvanostatic charge/discharge (GCD) profiles at rates between 20 – 5,000 mA/g are shown in **Fig. 6A-C**. The potential profiles at low rates are comparable for all samples, with variations in the maximum capacity. The samples show cathodic (lithiation) capacities at a rate of 20 mA/g with 169 mAh/g (V_2O_5-2C-DA), 193 mAh/g (V_2O_5-6C-DA) and 155 mAh/g (V_2O_5-12C-DA). However, at higher rates like 5 A/g, a reduced polarization is observed for V_2O_5-12C-DA compared to V_2O_5-2C-DA and V_2O_5-6C-DA, indicating improved kinetics for the V_2O_5 host with the largest interlayer spacing.

Cyclic voltammograms (CVs) at a rate of 10 mV/s give additional insights into the (de)lithiation process (**Fig. 6D**). While all (cathodic) lithiation peaks are roughly centered at around 2.6-2.7 V vs. Li^+/Li, the peak shapes become broader with increasing V_2O_5 interlayer spacing. Furthermore, the overpotential is reduced for V_2O_5-12C-DA, which shows the onset of the (anodic) delithiation peak at lower potentials compared to V_2O_5-2C-DA and V_2O_5-6C-DA, demonstrating improved electrochemical reversibility for V_2O_5-12C-DA at such a high sweep rate. Comparison with the CV of a bilayered Li-V_2O_5 reference sample shows significantly improved electrochemical reversibility, indicating improved kinetics for alkyldiamine-pillared samples compared to pre-intercalated Li^+.

Quantitative analysis of the capacity at different currents is probed by GCD at rates up to 5 A/g (**Fig. 6E**). The trends of improved kinetics for larger interlayer spacings are reflected in the capacity retention at higher rates, with V_2O_5-12C-DA showing the highest capacity retention of 50 mAh/g compared to 37 mAh/g (V_2O_5-6C-DA) and 23 mAh/g (V_2O_5-2C-DA) at a rate of 5 A/g. It should be noted that the reported values of specific capacity take into account the mass of both the V_2O_5 host and the alkyldiamine pillars, where the latter do not contribute to the reversible charge storage process. Thus, to gain fundamental insights into the charge storage process in pillared V_2O_5 hosts, quantification of stored Li^+ per structural unit of V_2O_5 is derived from the reversible, electrochemically stored charge and the quantity of pillars derived from TGA. Calculation of the maximum number of Li^+ stored yields stoichiometries of $Li_{1.02}V_2O_5$, $Li_{1.27}V_2O_5$-2C-DA, $Li_{1.48}V_2O_5$-6C-DA, and $Li_{1.33}V_2O_5$-C12-DA, demonstrating increased storage capacity of pillared V_2O_5 despite the additional presence of pillar molecules in the interlayer space.

The cycling stability of pillared V_2O_5 materials is probed by GCD at 0.5 A/g over 100 cycles and shown in **Fig. 6F**. All samples show a significant initial capacity decay over ca. 5-10 cycles and a slow but linear capacity reduction over the next 90 cycles, which is in line with other reports on lithium (de)intercalation in V_2O_5.[11,13] To probe whether the capacity decay is a consequence of the V_2O_5 host structure or disintegrating pillaring structure, ex situ XRD measurements of electrodes after 50 cycles are presented (**Fig. S3**). The diffractograms show that the initial interlayer spacing is retained, demonstrating that alkyldiamine pillars remain in the V_2O_5 structure. Consequently, future work with a focus on practical application will include the transfer of this pillaring approach to host systems that exhibit higher intrinsic cycling stability than bilayered V_2O_5, which is known for a limited long-term stability of Li^+ intercalation.[11]

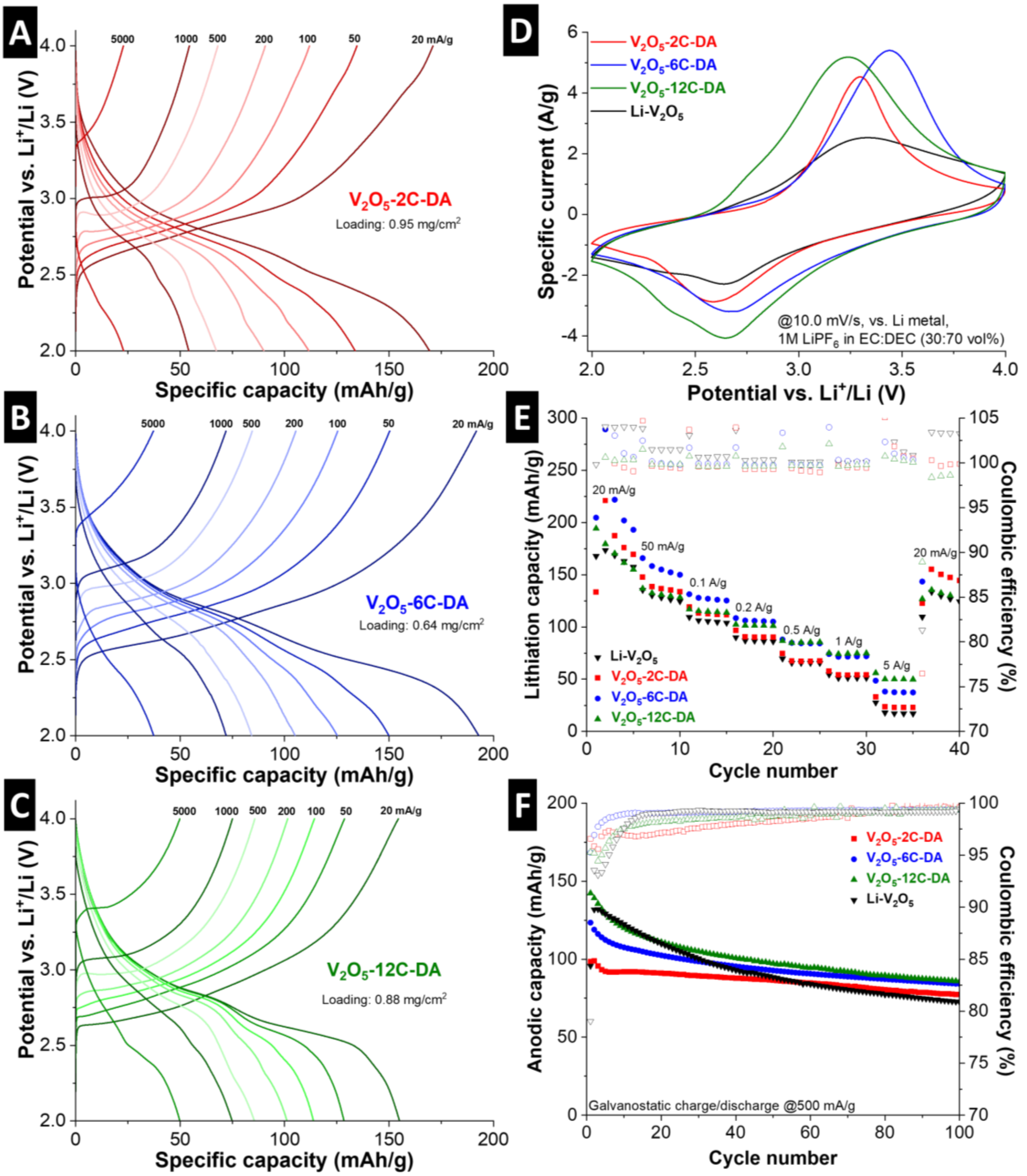

Figure 6: Galvanostatic charge/discharge profiles of (A) V_2O_5-2C-DA, (B) V_2O_5-6C-DA, (C) V_2O_5-12C-DA, at specific currents of 20, 50, 100, 200 and 500 mA/g. (D) Cyclic voltammograms of Li-V_2O_5, V_2O_5-2C-DA, V_2O_5-6C-DA and V_2O_5-12C-DA at a sweep rate of 10.0 mV/s. (E) Cathodic capacity from GCD for 5 cycles each at specific currents of 20, 50, 100, 200, 500, 1000 and 5000 mA/g. (F) Long term GCD at 500 mA/g. All measurements are conducted in coin cells versus Li metal electrodes in 1 M $LiPF_6$ in EC/DEC (30:70 vol.%) electrolyte. All mass-normalizations are with respect to the mass of the full V_2O_5-alkyldiamine composite.

To gain mechanistic insights into the electrochemical (de)lithiation process as a function of the nanoconfinement geometry of bilayered V_2O_5, the evolution of the (001) d-spacing of the electrode materials is studied by operando XRD over five consecutive cycles. For V_2O_5-2C-DA (**Fig. 7A**), at open circuit potential (OCP, ca. 3.5 V vs. Li^+/Li) the (001) signal is located at 4.0° 2θ (Mo Kα source), corresponding to a d-spacing of 1.02 nm in line with the pristine V_2O_5-2C-DA material. This excludes the possibility of spontaneous ion and/or solvent insertion into the host material that is not driven by an external electrochemical stimulation. Upon electrochemical reduction (lithiation) to 2.0 V vs. Li^+/Li and subsequent oxidation (delithiation) to 4.0 V vs. Li^+/Li, the position of the (001) signal continuously shifts with maxima between ca. 3.96° 2θ (lithiated) and 4.02° 2θ (delithiated). This indicates lithium (de)intercalation via a solid-solution mechanism associated with an almost negligible variation of d-spacing between 1.03 – 1.01 nm.

For V_2O_5-6C-DA (**Fig. 7B**), comparable behavior is observed with the position of the (001) signal at OCP centered at ca. 3.3° 2θ, corresponding to a d-spacing of 1.23 nm in line with the pristine V_2O_5-6C-DA material. At the same time, reversible and continuous shifts upon electrochemical reduction and oxidation to ca. 1.28 nm and 1.25 nm are observed, respectively, suggesting the same solid-solution lithium (de)intercalation mechanism as in V_2O_5-2C-DA. In both cases, the Li^+ intercalation-induced d-spacing changes of pillared V_2O_5-2C-DA and V_2O_5-6C-DA are very small and highly reversible over 5 consecutive cycles.

For V_2O_5-12C-DA (**Fig. 7C**), differences in the structural evolution of the host material are observed. At OCP, the material exhibits a (001) signal centered at ca. 2.3° 2θ corresponding to a d-spacing of 1.77 nm, which is slightly lower than that of the pristine V_2O_5-12C-DA material. During lithiation, an initial, abrupt increase in d-spacing to 2.04 nm is observed, followed by a further, more continuous increase to about 2.48 nm in the fully lithiated state at 2.0 V. Upon subsequent delithiation, contraction of the (001) d-spacing to 2.07 nm is observed and the behavior is highly reversible in the subsequent cycles. The abrupt expansion of the host during the first electrochemical reduction is indicative of significant structural changes induced by the intercalation of a large guest species. Such behavior is reminiscent of Li^+-solvent cointercalation behavior, for example, in $Ti_3C_2T_x$ MXene host electrodes.[63,64] We hypothesize that in the present case of V_2O_5-12C-DA, the large initial d-spacing allows for such an effect with solvent molecules from the electrolyte entering the interlayer space together with Li^+.[65]

To further investigate the hypothesized ion-solvent cointercalation mechanism in V_2O_5-12C-DA, ex situ XRD is carried out on a lithiated electrode material that is removed from the electrochemical cell at 2.0 V vs. Li^+/Li. Instead of the highly expanded d-spacing found during the operando experiment, a much smaller d-spacing of ca. 1.5 nm is found for the lithiated electrode in the ex situ setting (**Fig. S4**). It was previously found that co-intercalated solvent molecules are highly volatile and quickly evaporate upon removal of the electrode from the electrochemical cell.[66] Thus, the significant reduction of measured d-spacing for V_2O_5-12C-DA in the ex situ experiment compared to the operando setting is supportive of the cointercalation mechanism hypothesis because of solvent evaporation from the nanoconfined interlayer space.

An alternative explanation for the observed d-spacing of V_2O_5-12C-DA in the lithiated state is a change of the 12C-DA pillars' tilt angle arrangement to α_i of 62° (according to Fig. 2B), however, such a change in pillar tilt angles is not observed for 2C-DA or 6C-DA making this explanation less likely in our estimation. Future work will address quantitative investigation into the potential ion-solvent cointercalation mechanism triggered by the nanoconfinement geometry of V_2O_5-12C-DA, for example, by using a combination of electrochemical quartz crystal microbalance experiments and molecular dynamics simulation. The pillar-induced cointercalation behavior could provide significant kinetic advantages for multivalent ion intercalation or low temperature operation, where the desolvation step poses a significant energy barrier.[65]

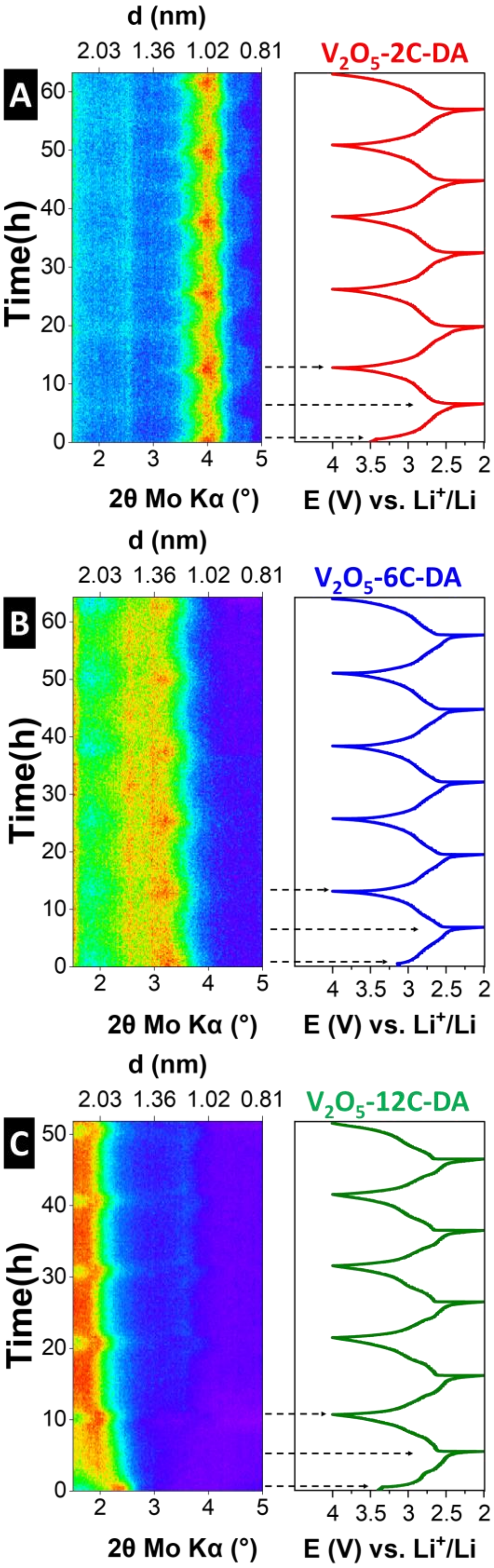

Figure 7: Electrochemical (de)lithiation mechanism studied via operando XRD (Mo Kα X-ray source, λ=0.71 Å) using a Debye-Scherrer (transmission) geometry in modified coin cells versus lithium metal over five consecutive galvanostatic charge/discharge cycles at a specific current of 50 mA/g. (A) V_2O_5-2C-DA, (B) V_2O_5-6C-DA, and (C) V_2O_5-12C-DA.

3.3 Computational investigation

First-principles calculations within the framework of Density Functional Theory (DFT) are conducted to gain a deeper understanding of the thermodynamics and kinetics involved in the Li^+ intercalation process in bilayered V_2O_5 intercalation hosts as a function of their nanoconfinement geometry, i.e., interlayer spacing. In our preliminary model construction, we adopt the crystal structure observed for $V_2O_5{\cdot}nH_2O$ again according to the model of Petkov et al.[44] As described in the structural characterization section, this structure exhibits bilayers of V_2O_5 arranged in a stacking fashion along the *c*-axis within a monoclinic unit cell (space group C2/m). These layers are composed of square pyramidal VO_5 units as shown in **Fig. 8A-B**. The interlayer distance expands or contracts as the guest ions or molecules intercalate within the bilayered framework.

The first step is the construction of an intercalant-free interlayer structure, with subsequent optimization based on DFT calculations, resulting in 0.87 nm interlayer spacing, and a interlayer gap between the two individual layers of V_2O_5 of approximately 0.29 nm. Details on the precise unit cell parameters utilizing different functionals are provided in **Table S1**.

To simulate the interlayer-expanded V_2O_5 structures, a set of varied interlayer distances of bilayered V_2O_5 is utilized, omitting the pillar molecules from the theoretical calculation for simplicity. This approach is a reasonable approximation, given the comparable occupational density and arrangement of alkyldiamine pillar molecules used in the experimental study, as well as their inactivity towards the electrochemical charge storage process. The chosen d-spacing of 1.21 nm corresponds to the “intermediate sample” V_2O_5-6C-DA. The d-spacing of 1.50 nm corresponds to the lithiated state of V_2O_5-12C-DA obtained from ex situ XRD (**Fig. S4**), representing the maximum expansion in the lithiated state without co-intercalated solvent from the electrolyte.

The investigation starts by analyzing the impact of increased interlayer spacing on the characteristics of Li^+ diffusion pathways within molecular pillar-free V_2O_5, utilizing the Bond Valence Site Energy (BVSE) approach as shown in **Fig. 8A**. According to the static BVSE model, there are 1D diffusion pathways for Li^+ sites with interlayer spacing of 0.87 nm. However, an increase in interlayer spacing facilitates the connection between channels, resulting in the formation of a 2D network of Li^+ pathways. Interestingly, the diffusion pathways for the system with an increase in interlayer spacing to 1.21 nm illustrate interactions with oxygen in a non-equivalent manner, adhering predominantly to one side, thereby facilitating a diffusion process more akin to surface diffusion (**Fig. 8B**).

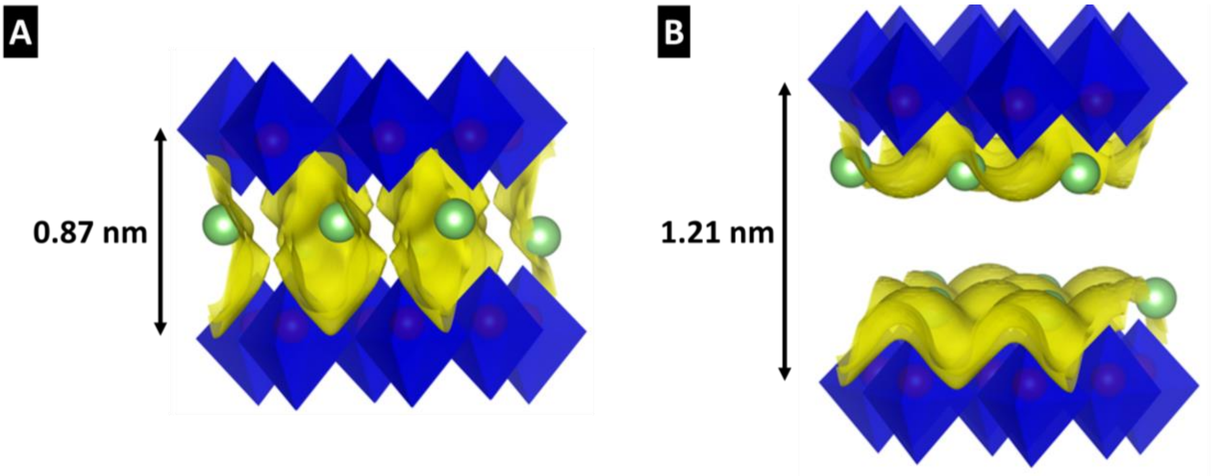

Figure 8: Simulated Bond Valence Site Energy (BVSE) profiles comparing the pristine compound with the compound following an increase in interlayer spacing. Green spheres represent lithium atoms, while blue octahedrons depict vanadium atoms coordinated by oxygen in an octahedral fashion. The yellow surfaces illustrate pathways for Li^+ diffusion. The isovalue is set to 0.08 e/Å³.

Further investigation is conducted into the mechanism of Li^+ diffusion using Nudged Elastic Band (NEB) calculations within the framework of periodic DFT. The focus is on the effect of interlayer spacing in a dilute limit without pillar molecules. Initially, the Li-free V_2O_5 structure with a d-spacing of 0.87 nm is employed to assess the diffusion mechanisms and their activation barriers. Subsequently, the diffusion mechanisms and barriers for d-spacings of 1.21 nm and 1.50 nm are examined. Three distinct diffusion pathways are identified. Diffusion pathway 1 connects two pyramidal Li^+ sites, each initially exhibiting a 5-fold coordination environment, with three oxygen atoms on one side and two on the opposite side of the layers (**Fig. 9A-C**). Note that both sites are more prominently bound (three vs. two coordinating oxygen atoms) to opposite V_2O_5 bilayers. As the interlayer spacing increases, the two oxygen atoms from the upper layer are no longer capable of forming bonds, reducing the coordination number from 5-fold to 3-fold, as illustrated in **Fig. 9B-C**. In addition, the diffusion of Li^+ along this pathway entails traversing the interlayer space in between the V_2O_5 bilayers in which an effective coordination of Li^+ ion is no longer maintained (**Fig. S5**). This, in turn, leads to the formation of high diffusion barriers (>1 eV), which excludes this pathway from contributing to Li^+ conductivity (**Fig. 9D**).

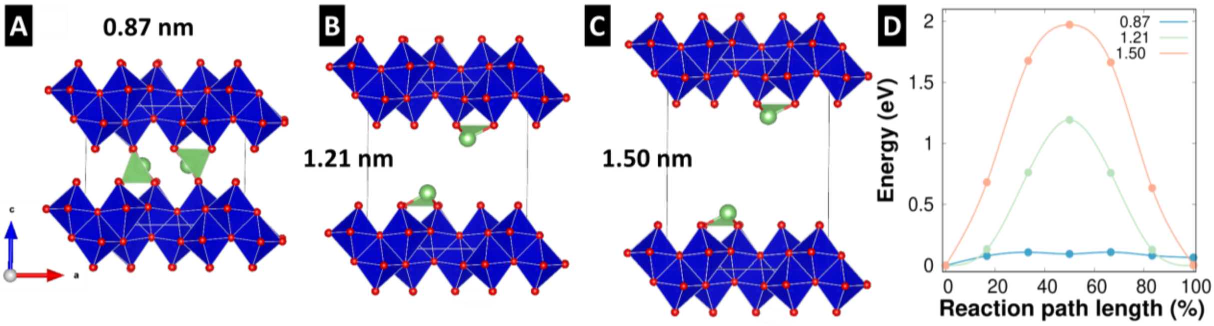

Figure 9: Side view of the initial and final state of the diffusion pathway 1 for increasing d-spacings of (A) 0.87 nm, (B) 1.21 nm, and (C) 1.50 nm. (D) Energy barriers (in eV) for Li^+ diffusion plotted against the reaction path coordinate, obtained via periodic DFT calculations in combination with nudged elastic band (NEB) method. NEB results illustrating the energy profiles for the pristine material (shown in blue) and the material with increasing interlayer spacing of 1.21 nm and 1.50 nm, represented by green and orange, respectively.

Diffusion pathway 2, which commences at an initially 4-fold coordination site, coordinated by three oxygen atoms in the upper layer and only one oxygen atom in the bottom layer (**Fig. 10A**), demonstrates an invariant activation barrier (0.14-0.15 eV) due to a change in diffusion mechanism when the interlayer spacing increased (**Fig. 10D**). For an interlayer spacing of 0.87 nm, the initial site is 0.15 eV higher in energy than the final site and the diffusion pathway involves two intermediate sites. The first intermediate site is equivalent to the final 5-fold coordination, however, predominantly bound to the bottom layer and thus corresponds to traversing the empty space in between. The second intermediate is analogous to that observed in the first pathway, which exhibits planar 4-fold coordination. However, as the interlayer spacing increases, the diffusion mechanism undergoes a transformation (**Fig. 10B-C**). This is due to the inability of oxygen atoms from the opposing side of the layer to serve as effective coordinators and the corresponding large barrier for Li^+ to jump to the opposing side, thus minimizing the site preference of the initial and final states. These findings demonstrate that Li^+ diffusion along a single site of the V_2O_5 bilayer is facilitated by a change in its operational mode as the interlayer spacing increases.

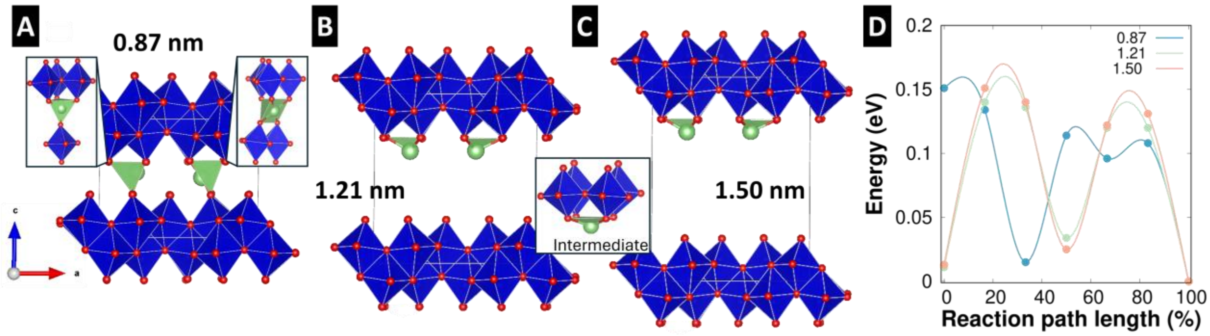

Figure 10: Side view of the initial and final state of the diffusion pathway 2 for increasing d-spacings of (A) 0.87 nm, (B) 1.21 nm, and (C) 1.50 nm. The insets in (A) highlight the difference in coordination environment between initial 4-fold coordination (left) and final 5-fold coordination (right). The inset in (B) and (C) shows the coordination of the intermediate site of the diffusion pathway. (D) Energy barriers (in eV) for Li^+ diffusion plotted against the reaction path coordinate, obtained via periodic DFT calculations in combination with NEB method.

Diffusion pathway 3, which involves surface-like diffusion along pyramidal 5-fold coordination sites predominantly bound to the same layer (**Fig. 11**), also shifts to a mechanism similar to the second pathway. In the case of the pristine structure with an interlayer spacing of 0.87 nm, the diffusion pathway involves a transition state with short bond distances (d=1.75 Å) to oxygen atoms from the opposing layer (**Fig. 11A**) and high activation barriers of 0.51 eV. When the interlayer spacing increases, a 4-fold intermediate site emerges instead, leading to a shift in mechanism and low diffusion barriers (0.14-0.17 eV) (**Fig. 11D**).

Overall, the study reveals that increasing the interlayer spacing introduces a complex interplay between bond distance and coordination environments, affecting the diffusion barriers and mechanisms. Diffusion pathways traversing the interlayer space are hindered by severe undercoordination, while an alternative surface-like diffusion mechanism with low activation barriers becomes activated. This new mechanism is characterized by minimal site preference for initial, final, and intermediate sites, leading to lower activation barriers, which has implications for improving Li^+ conductivity in similar layered materials.

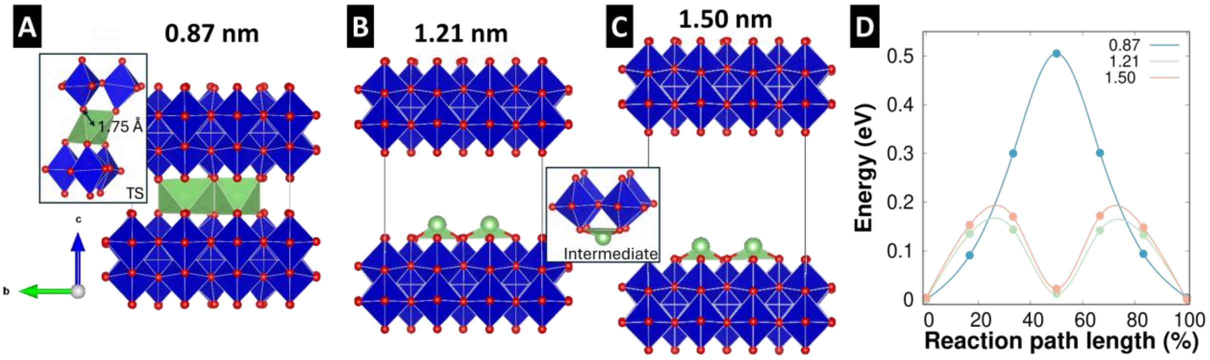

Figure 11: Side view of the initial and final state of the diffusion pathway 3 for increasing d-spacings of (A) 0.87 nm, (B) 1.21 nm, and (C) 1.50 nm. The inset in (A) shows the transition state configuration characterized by a 5-fold coordination of the Li ion. The short bond distance of 1.75 Å is much shorter than the sum of the ionic radii of O^{2-} (1.4 Å) and Li^+ (0.76 Å) and leads to substantial diffusion barriers of E_a = 0.51 eV for a d-spacing of 8.6 Å. The inset in (B) and (C) shows the coordination of the intermediate site of the diffusion pathway. (D) Energy barriers (in eV) for Li^+ diffusion plotted against the reaction path coordinate, obtained via periodic DFT calculations in combination with NEB method.

4. Conclusions

A series of bilayered V_2O_5 host materials with well-defined interlayer spacings between 1.0-1.9 nm is synthesized. This is owing to the introduction of alkyldiamine molecular pillars of different lengths. Detailed structural characterization, including high resolution TEM at length scales relevant to the hosts' nanoconfinement geometries, reveals the structural properties of pillared V_2O_5 in detail. The materials exhibit comparable nanowhisker morphology, intralayer crystal structure, specific surface area, tilted pillar conformation and ionic host-pillar interaction, thus only varying in *c*-lattice parameter. This allows to unambiguously link their functional properties to the variation of nanoconfinement geometry.

The maximum specific capacity for Li^+ intercalation in the host materials at low rate is between 155 – 193 mAh/g. Subtracting the mass contribution of (electrochemically) inactive pillaring molecules, the lithium ion storage capacity per V_2O_5 is increased with larger interlayer spacing, with an improvement from approx. 1.0 to 1.5 Li^+ in the material with the intermediate expansion. Furthermore, the rate handling improves with larger interlayer spacings. This demonstrates the possibility of improving ion storage capacity and kinetics in layered host materials by manipulating the nanoconfinement geometry. Density functional theory investigations explain the kinetic properties by a change in diffusion mechanism from 1D towards networks of 2D diffusional pathways for Li^+ when increasing the interlayer spacing of V_2O_5 hosts. Operando X-ray diffraction investigation reveals a solid-solution Li^+ intercalation mechanism with minimal reversible expansion/contraction behavior for V_2O_5 hosts with small (V_2O_5-2C-DA) and intermediate (V_2O_5-6C-DA) interlayer spacing. For V_2O_5 with the largest interlayer spacing (V_2O_5-12C-DA), an abrupt further expansion is observed. We hypothesize this is due to the simultaneous intercalation of electrolyte solvent (ion-solvent cointercalation mechanism). This demonstrates the dependence of the charge storage mechanism on the host material's nanoconfinement geometry.

Overall, the work provides systematic insights into the structural properties and associated functionality of pillared V_2O_5 materials serving as ion intercalation hosts, which is of relevance to research into high power energy storage or multivalent ion intercalation cathodes. Insights gained into materials providing a well-defined nanoconfinement geometry is also of interest to electrocatalysis or ion selectivity.

Acknowledgements

J.K., E.V. and S.F. acknowledge funding from the German Federal Ministry of Education and Research (BMBF) in the "NanoMatFutur" program (grant No. 03XP0423). S.F. would like to thank the Daimler and Benz Foundation for financial support in the Scholarship program. The authors thank Adam Reupert (HIU) for helpful discussions and acknowledge financial support from the Helmholtz Association. C.O. and B.B. acknowledge the DFG-funded Micro-and Nanoanalytics Facility (MNaF) of the University of Siegen (INST 221/131-1) for utilizing its major TEM instrument FEI Talos F200X (DFG INST 221/93-1, DFG INST 221/126-1). Financial support by the German Research Foundation (DFG) through Project ID 390 874 152 (EXC 2154, POLiS Cluster of Excellence) is gratefully acknowledged. The authors furthermore acknowledge computer time provided by the state of Baden-Württemberg through the bwHPC program and the German Research Foundation (DFG) through Grant no. INST 40/575-1 FUGG (JUSTUS 2 cluster). This work contributes to the research performed at CELEST (Center for Electrochemical Energy Storage Ulm-Karlsruhe).

Conflicts of interest

The authors have no conflicts to declare.

References

(1.) Luo, Y.; Bai, Y.; Mistry, A.; Zhang, Y.; Zhao, D.; Sarkar, S.; Handy, J. V; Rezaei, S.; Chuang, A. C.; Carrillo, L.; Wiaderek, K.; Pharr, M.; Xie, K.; Mukherjee, P. P.; Xu, B.; Banerjee, S. Effect of Crystallite Geometries on Electrochemical Performance of Porous Intercalation Electrodes by Multiscale Operando Investigation. *Nat. Mater.* **2022**, 21, 217–227.

(2.) Choi, J.; Moon, H.; Fleischmann, S. Simultaneous Control of Crystallite Size and Interlayer Spacing of MoS2 to Achieve Pseudocapacitive Lithium Intercalation. *Electrochim. Acta* **2024**, 476, 143774.

(3.) Lv, R.; Luo, C.; Liu, B.; Hu, K.; Wang, K.; Zheng, L.; Guo, Y.; Du, J.; Li, L.; Wu, F.; Chen, R. Unveiling Confinement Engineering for Achieving High-Performance Rechargeable Batteries. *Adv. Mater.* **2024**, 36, 2400508.

(4.) Fleischmann, S.; Mitchell, J. B.; Wang, R.; Zhan, C.; Jiang, D. E.; Presser, V.; Augustyn, V. Pseudocapacitance: From Fundamental Understanding to High Power Energy Storage Materials. *Chem. Rev.* **2020**, 120, 6738–6782.

(5.) Clites, M.; W. Byles, B.; Pomerantseva, E. Bilayered Vanadium Oxide as the Host Material for Reversible beyond Lithium Ion Intercalation. *Adv. Mater. Lett.* **2017**, 8, 679–688.

(6.) Fu, Q.; Zhao, H.; Sarapulova, A.; Dsoke, S. V2O5 as a Versatile Electrode Material for Postlithium Energy Storage Systems. *Appl. Res.* **2022**, 2, e202200070.

(7.) Moretti, A.; Passerini, S. Bilayered Nanostructured V2O5·nH2O for Metal Batteries. *Adv. Energy Mater.* **2016**, 6, 1600868.

(8.) Fleischmann, S.; Spencer, M. A.; Augustyn, V. Electrochemical Reactivity under Confinement Enabled by Molecularly Pillared 2D and Layered Materials. *Chem. Mater.* **2020**, 32, 3325–3334.

(9.) Li, M.; Fan, Q.; Gao, L.; Liang, K.; Huang, Q. Chemical Intercalation of Layered Materials: From Structure Tailoring to Applications. *Adv. Mater.* **2024**, 2312918.

(10.) Augustyn, V. Tuning the Interlayer of Transition Metal Oxides for Electrochemical Energy Storage. *J. Mater. Res.* **2017**, 32, 2–15.

(11.) Clites, M.; Pomerantseva, E. Bilayered Vanadium Oxides by Chemical Pre-Intercalation of Alkali and Alkali-Earth Ions as Battery Electrodes. *Energy Storage Mater.* **2018**, 11, 30–37.

(12.) Wei, Q.; Jiang, Z.; Tan, S.; Li, Q.; Huang, L.; Yan, M.; Zhou, L.; An, Q.; Mai, L. Lattice Breathing Inhibited Layered Vanadium Oxide Ultrathin Nanobelts for Enhanced Sodium Storage. *ACS Appl. Mater. Interfaces* **2015**, 7, 18211–18217.

(13.) Luo, Y.; Handy, J. V.; Das, T.; Ponis, J. D.; Albers, R.; Chiang, Y. H.; Pharr, M.; Schultz, B. J.; Gobbato, L.; Brown, D. C.; Chakraborty, S.; Banerjee, S. Effect of Pre-Intercalation on Li-Ion Diffusion Mapped by Topochemical Single-Crystal Transformation and Operando Investigation. *Nat. Mater.* **2024**, https://doi.org/10.1038/s41563-024-01842-y.

(14.) Liu, C.; Neale, Z.; Zheng, J.; Jia, X.; Huang, J.; Yan, M.; Tian, M.; Wang, M.; Yang, J.; Cao, G. Expanded Hydrated Vanadate for High-Performance Aqueous Zinc-Ion Batteries. *Energy Environ. Sci.* **2019**, 12, 2273.

(15.) Zhang, S.; Chen, L.; Dong, D.; Kong, Y.; Zhang, J.; Liu, J.; Liu, Z. AmV2O5 with Binary Phases as High-Performance Cathode Materials for Zinc-Ion Batteries: Effect of the Pre-Intercalated Cations A and Reversible Transformation of Coordination Polyhedra. *ACS Appl. Mater. Interfaces* **2022**, 14, 24415–24424.

(16.) Tian, M.; Liu, C.; Zheng, J.; Jia, X.; Jahrman, E. P.; Seidler, G. T.; Long, D.; Atif, M.; Alsalhi, M.; Cao, G. Structural Engineering of Hydrated Vanadium Oxide Cathode by K+ Incorporation for High-Capacity and Long-Cycling Aqueous Zinc Ion Batteries. *Energy Storage Mater.* **2020**, 29, 9–16.

(17.) Tolstopyatova, E. G.; Kamenskii, M. A.; Kondratiev, V. V. Vanadium Oxide–Conducting Polymers Composite Cathodes for Aqueous Zinc-Ion Batteries: Interfacial Design and Enhancement of Electrochemical Performance. *Energies* **2022**, 15.

(18.) Feng, Z.; Sun, J.; Liu, Y.; Jiang, H.; Hu, T.; Cui, M.; Tian, F. Polypyrrole-Intercalation Tuning Lamellar Structure of V2O5·nH2O Boosts Fast Zinc-Ion Kinetics for Aqueous Zinc-Ion Battery. *J. Power Sources* **2022**, 536, 231489.

(19.) He, W.; Fan, Z.; Huang, Z.; Liu, X.; Qian, J.; Ni, M.; Zhang, P.; Hu, L.; Sun, Z. M. A Li+ and PANI Co-Intercalation Strategy for Hydrated V2O5 to Enhance Zinc Ion Storage Performance. *J. Mater. Chem. A* **2022**, 10, 18962–18971.

(20.) Wang, Z.; Tang, X.; Yuan, S.; Bai, M.; Wang, H.; Liu, S.; Zhang, M.; Ma, Y. Engineering Vanadium Pentoxide Cathode for the Zero-Strain Cation Storage via a Scalable Intercalation-Polymerization Approach. *Adv. Funct. Mater.* **2021**, 31, 2100164.

(21.) Xu, L.; Zhang, Y.; Zheng, J.; Jiang, H.; Hu, T.; Meng, C. Ammonium Ion Intercalated Hydrated Vanadium Pentoxide for Advanced Aqueous Rechargeable Zn-Ion Batteries.

Mater. Today Energy **2020**, 18.

(22.) Li, Y.; Zhang, S.; Wang, S.; Xiao, Z.; Meng, F.; Li, Q.; Zhang, X.; Zhang, Z.; Zhi, L.; Tang, Z. Layered Structure Regulation for Zinc-Ion Batteries: Rate Capability and Cyclability Enhancement by Rotatable Pillars. *Adv. Energy Mater.* **2023**, 2203810.

(23.) Sotoudeh, M.; Groß, A. Descriptor and Scaling Relations for Ion Mobility in Crystalline Solids. *JACS Au* **2022**, 2, 463–471.

(24.) Sotoudeh, M.; Baumgart, S.; Dillenz, M.; Döhn, J.; Forster-Tonigold, K.; Helmbrecht, K.; Stottmeister, D.; Groß, A. Ion Mobility in Crystalline Battery Materials. *Adv. Energy Mater.* **2024**, 14.

(25.) Wordsworth, J.; Benedetti, T. M.; Somerville, S. V; Schuhmann, W.; Tilley, R. D.; Gooding, J. J. The Influence of Nanoconfinement on Electrocatalysis. *Angew. Chemie - Int. Ed.* **2022**, 61, e202200755.

(26.) Shen, J.; Liu, G.; Han, Y.; Jin, W. Artificial Channels for Confined Mass Transport at the Sub-Nanometre Scale. *Nat. Rev. Mater.* **2021**, 6, 294–312.

(27.) Biesinger, M. C. Accessing the Robustness of Adventitious Carbon for Charge Referencing (Correction) Purposes in XPS Analysis: Insights from a Multi-User Facility Data Review. *Appl. Surf. Sci.* **2022**, 597, 153681.

(28.) Walton, J.; Wincott, P.; Fairley, N.; Carrick, A. *Peak Fitting with CasaXPS: A Casa Pocket Book*; Accolyte Science, **2010**.

(29.) Perdew, J. P.; Burke, K.; Ernzerhof, M. Generalized Gradient Approximation Made Simple. *Phys. Rev. Lett.* **1996**, 77, 3865–3868.

(30.) Sun, J.; Ruzsinszky, A.; Perdew, J. Strongly Constrained and Appropriately Normed Semilocal Density Functional. *Phys. Rev. Lett.* **2015**, 115, 036402.

(31.) Heyd, J.; Scuseria, G. E.; Ernzerhof, M. Hybrid Functionals Based on a Screened Coulomb Potential. *J. Chem. Phys.* **2003**, 118, 8207–8215.

(32.) Krukau, A. V.; Vydrov, O. A.; Izmaylov, A. F.; Scuseria, G. E. Influence of the Exchange Screening Parameter on the Performance of Screened Hybrid Functionals. *J. Chem. Phys.* **2006**, 125, 224106.

(33.) Joubert, D. From Ultrasoft Pseudopotentials to the Projector Augmented-Wave Method. *Phys. Rev. B - Condens. Matter Mater. Phys.* **1999**, 59, 1758–1775.

(34.) Blöchl, P. E. Projector Augmented-Wave Method. *Phys. Rev. B* **1994**, 50, 17953–17979.

(35.) Grimme, S.; Antony, J.; Ehrlich, S.; Krieg, H. A Consistent and Accurate Ab Initio Parametrization of Density Functional Dispersion Correction (DFT-D) for the 94

Elements H-Pu. *J. Chem. Phys.* **2010**, 132, 154104.

(36.) Sabatini, R.; Gorni, T.; De Gironcoli, S. Nonlocal van Der Waals Density Functional Made Simple and Efficient. *Phys. Rev. B - Condens. Matter Mater. Phys.* **2013**, 87, 041108.

(37.) Peng, H.; Yang, Z. H.; Perdew, J. P.; Sun, J. Versatile van Der Waals Density Functional Based on a Meta-Generalized Gradient Approximation. *Phys. Rev. X* **2016**, 6, 041005.

(38.) Wang, L.; Maxisch, T.; Ceder, G. Oxidation Energies of Transition Metal Oxides within the GGA+U Framework. *Phys. Rev. B - Condens. Matter Mater. Phys.* **2006**, 73, 1–6.

(39.) Artrith, N.; Garrido Torres, J. A.; Urban, A.; Hybertsen, M. S. Data-Driven Approach to Parameterize SCAN+U for an Accurate Description of 3d Transition Metal Oxide Thermochemistry. *Phys. Rev. Mater.* **2022**, 6, 035003.

(40.) Pack, J. D.; Monkhorst, H. J. Special Points for Brillouin-Zone Integrations. *Phys. Rev. B* **1977**, 16, 1748–1749.

(41.) Henkelman, G.; Jónsson, H. Improved Tangent Estimate in the Nudged Elastic Band Method for Finding Minimum Energy Paths and Saddle Points. *J. Chem. Phys.* **2000**, 113, 9978–9985.

(42.) Henkelman, G.; Uberuaga, B. P.; Jónsson, H. A Climbing Image Nudged Elastic Band Method for Finding Saddle Points and Minimum Energy Paths. *J. Chem. Phys.* **2000**, 113, 9901–9904.

(43.) Jain, A.; Ong, S. P.; Hautier, G.; Chen, W.; Richards, W. D.; Dacek, S.; Cholia, S.; Gunter, D.; Skinner, D.; Ceder, G.; Persson, K. A. Commentary: The Materials Project: A Materials Genome Approach to Accelerating Materials Innovation. *APL Mater.* **2013**, 1, 011002.

(44.) Petkov, V.; Trikalitis, P. N.; Bozin, E. S.; Billinge, S. J. L.; Vogt, T.; Kanatzidis, M. G. Structure of V2O5·nH2O Xerogel Solved by the Atomic Pair Distribution Function Technique. *J. Am. Chem. Soc.* **2002**, 124, 10157–10162.

(45.) Chen, D.; Liu, M.; Yin, L.; Li, T.; Yang, Z.; Li, X.; Fan, B.; Wang, H.; Zhang, R.; Li, Z.; Xu, H.; Lu, H.; Yang, D.; Sun, J.; Gao, L. Single-Crystalline MoO3 Nanoplates: Topochemical Synthesis and Enhanced Ethanol-Sensing Performance. *J. Mater. Chem.* **2011**, 21, 9332–9342.

(46.) Zhou, C.; Wang, D.; Lagunas, F.; Atterberry, B.; Lei, M.; Hu, H.; Zhou, Z.; Filatov, A. S.; Jiang, D.; Rossini, A. J.; Klie, R. F.; Talapin, D. V. Hybrid Organic–Inorganic Two-Dimensional Metal Carbide MXenes with Amido- and Imido-Terminated Surfaces. *Nat.*

Chem. **2023**, 15, 1722–1729.

(47.) Ha, B.; Char, K. Conformational Behavior of Dodecyldiamine inside the Confined Space of Montmorillonites. *Langmuir* **2005**, 21, 8471–8477.

(48.) Datta, S.; Jo, C.; Volder, M. De; Torrente-Murciano, L. Morphological Control of Nanostructured V2O5 by Deep Eutectic Solvents. *ACS Appl. Mater. Interfaces* **2020**, 12, 18803–18812.

(49.) Fei, H.-L.; Zhou, H.-J.; Wang, J.-G.; Sun, P.-C.; Ding, D.-T.; Chen, T.-H. Synthesis of Hollow V2O5 Microspheres and Application to Photocatalysis. *Solid State Sci.* **2008**, 10, 1276–1284.

(50.) Si, H.; Seidl, L.; Chu, E. M. L.; Martens, S.; Ma, J.; Qiu, X.; Stimming, U.; Schneider, O. Impact of the Morphology of V2O5 Electrodes on the Electrochemical Na+-Ion Intercalation. *J. Electrochem. Soc.* **2018**, 165, A2709–A2717.

(51.) Zheng, J.; Zhang, Y.; Hu, T.; Lv, T.; Meng, C. New Strategy for the Morphology-Controlled Synthesis of V2O5 Microcrystals with Enhanced Capacitance as Battery-Type Supercapacitor Electrodes. *Cryst. Growth Des.* **2018**, 18, 5365–5376.

(52.) Shin, Y.; Stepien, D.; Hepp, M.; Butz, B.; Bresser, D.; Fleischmann, S. Cryogenic Electron Microscopy Workflows for the Characterization of Electrochemical Interfaces and Interphases in Batteries. *J. Power Sources* **2023**, 556, 232515.

(53.) Zhang, D. R.; Kim, C. W.; Kang, Y. S. A Study on the Crystalline Structure of Sodium Titanate Nanobelts Prepared by the Hydrothermal Method. *J. Phys. Chem. C* **2010**, 114, 8294–8301.

(54.) Liu, Y.; Clark, M.; Zhang, Q.; Yu, D.; Liu, D.; Liu, J.; Cao, G. V2O5 Nano-Electrodes with High Power and Energy Densities for Thin Film Li-Ion Batteries. *Adv. Energy Mater.* **2011**, 1, 194–202.

(55.) Sediri, F.; Gharbi, N. From Crystalline V2O5 to Nanostructured Vanadium Oxides Using Aromatic Amines as Templates. *J. Phys. Chem. Solids* **2007**, 68, 1821–1829.

(56.) Brunauer, S.; Emmett, P. H.; Teller, E. Adsorption of Gases in Multimolecular Layers. *J. Am. Chem. Soc.* **1938**, 60, 309–319.

(57.) Thommes, M.; Kaneko, K.; Neimark, A. V.; Olivier, J. P.; Rodriguez-Reinoso, F.; Rouquerol, J.; Sing, K. S. W. Physisorption of Gases, with Special Reference to the Evaluation of Surface Area and Pore Size Distribution (IUPAC Technical Report). *Pure Appl. Chem.* **2015**, 87, 1051–1069.

(58.) Reddy, B. M.; Khan, A.; Yamada, Y.; Kobayashi, T.; Loridant, S.; Volta, J.-C. Surface

Characterization of CeO2/SiO2 and V2O5/CeO2/SiO2 Catalysts by Raman, XPS, and Other Techniques. *J. Phys. Chem. B* **2002**, 106, 10964–10972.

(59.) Biesinger, M. C.; Lau, L. W. M.; Gerson, A. R.; Smart, R. S. C. Resolving Surface Chemical States in XPS Analysis of First Row Transition Metals, Oxides and Hydroxides: Sc, Ti, V, Cu and Zn. *Appl. Surf. Sci.* **2010**, 257, 887–898.

(60.) Wagner, C. D.; Naumkin, A. V; Kraut-Vass, A.; Allison, J. W.; Powell, C. J.; Rumble Jr, J. R. NIST Standard Reference Database 20. http:/srdata.nist.gov/xps/ 2023.

(61.) Crist, B. V. *Handbooks of Monochromatic XPS Spectra: Volume 2: Commercially Pure Binary Oxides*; XPS International LLC, **2004**.

(62.) Beamson, G.; Briggs, D. R. High Resolution XPS of Organic Polymers: The Scienta ESCA300 Database; **1992**.

(63.) Wang, X.; Mathis, T. S.; Li, K.; Lin, Z.; Vlcek, L.; Torita, T.; Osti, N. C.; Hatter, C.; Urbankowski, P.; Sarycheva, A.; Tyagi, M.; Mamontov, E.; Simon, P.; Gogotsi, Y. Influences from Solvents on Charge Storage in Titanium Carbide MXenes. *Nat. Energy* **2019**, 4, 241–248.

(64.) Wang, X.; Mathis, T. S.; Sun, Y.; Tsai, W. Y.; Shpigel, N.; Shao, H.; Zhang, D.; Hantanasirisakul, K.; Malchik, F.; Balke, N.; Jiang, D. E.; Simon, P.; Gogotsi, Y. Titanium Carbide MXene Shows an Electrochemical Anomaly in Water-in-Salt Electrolytes. *ACS Nano* **2021**, 15, 15274–15284.

(65.) Guo, H.; Elmanzalawy, M.; Sivakumar, P.; Fleischmann, S. Unifying Electrolyte Formulation and Electrode Nanoconfinement Design to Enable New Ion – Solvent Cointercalation Chemistries. *Energy Environ. Sci.* **2024**, 17, 2100–2116.

(66.) Åvall, G.; A. Ferrero, G.; Janßen, K. A.; Exner, M.; Son, Y.; Adelhelm, P.; Ferrero, G. A.; Janßen, K. A.; Exner, M.; Son, Y. In Situ Pore Formation in Graphite Through Solvent Co-Intercalation : A New Model for The Formation of Ternary Graphite Intercalation Compounds Bridging Batteries and Supercapacitors. *Adv. Energy Mater.* **2023**, 13, 2301944.